Renewable Energy 198 (2022) 1210–1223

Contents lists available at ScienceDirect

Renewable Energy

journal homepage: www.elsevier.com/locate/renene

Evaluation of discharging performance of molten salt/ceramic foam composite phase change material in a shell-and-tube latent heat thermal energy storage unit

Shuai Zhang, Yuying Yan *

Faculty of Engineering, University of Nottingham, University Park, Nottingham, UK

ARTICLE INFO

Keywords:
Molten salt
Solar power
Thermal energy storage
Ceramic foam
Heat transfer enhancement
Discharging

ABSTRACT

Molten salts are widely used energy storage media in integrated solar power systems, however, due to their high corrosivity and the extreme high-temperature environment, many current methods of heat transfer enhancement do not apply. Herein, we proposed to use ceramic foam to enhance the discharging performance of molten salt to efficiently supply heat for power generation. The ceramic foam was prepared and its corrosion resistance was confirmed experimentally. The discharging performance in a shell-and-tube latent heat thermal energy storage unit was numerically studied. It is found that compared to the configuration without enhancement, the solidification time of the ceramic foam-enhanced unit is shortened by up to 52.0%. The unit with the upper foam insert shows better discharging performance than the one with the lower foam insert. Different foam filling height is also considered and results indicate that the thermal energy release rate always increases with the foam filling height and that of the fully foam-inserted unit is 118.1% higher than that of the none foam-inserted unit. For the first time, the discharging performance of ceramic foam-enhanced molten salt is quantitatively evaluated. This study provides guidance on designing thermal energy storage sub-system with excellent heat supply performance for solar power generation.

1. Introduction

Reducing greenhouse gas emissions to net zero is imperative to stop global warming and safeguard a liveable climate [1]. Using renewable energy is one of the solutions to cut greenhouse gas emissions [2,3]. Solar energy, as an essential source of renewable energy, has great potential to generate electricity [4,5]. On the one hand, it increases the energy supply due to the abundance, which relieves the global energy crisis; on the other hand, solar power does not generate greenhouse gases, which helps stop global warming. Concentrated solar power (CSP) technology converts solar radiation to heat and then to power. Compared to photovoltaic (PV), it is less cost-effective, but it has specific advantages, mainly in storage. First, to address the discontinuous power generation, in CSP, thermal energy is stored, while in PV, electrical energy is stored (in batteries). The cost of thermal energy storage is lower and more environmentally friendly than electrical energy storage in PV [6]. Second, the thermal energy storage system can store enough heat to enable CSP to cover not only the peak load but also the base load. However, in PV, no such large storage which can meet the base load is technically feasible [6,7]. Organic Rankine Cycle (ORC) is a widely recognised technology to convert solar heat into power at the temperature of 400 °C or lower [4]. Compared to the conventional steam Rankine cycle at low-to-medium temperature ($<400\,^{\circ}$C), the advantages of ORC-CSP include high turbine efficiency, low mechanical stress, low operation and maintenance costs and long plant life [8]. However, solar radiation has unsteady and intermittent nature, which results in ORC operating under off-design conditions with low efficiency [9]. This problem is solved by integrating the latent heat thermal energy storage (LHTES) into ORC [10]. LHTES stores unsteady solar radiation in phase change materials (PCMs) and then supplies steady heat to the ORC sub-system to generate power, maintaining ORC operating under design conditions [11,12].

Molten salts are widely used PCMs in integrated solar power systems due to their appropriate melting point, excellent chemical stability, high energy storage density, etc [13,14]. Some people have studied the integrated ORC solar power systems. Cioccolanti et al. [15] used solar salt (60%wt $NaNO_3$ + 40%wt KNO_3) as PCM and investigated a small-scale concentrated solar ORC plant. They found that the plant could achieve a high conversion efficiency when the ORC sub-system was supplied by

---

* Corresponding author.
E-mail address: Yuying.Yan@nottingham.ac.uk (Y. Yan).

https://doi.org/10.1016/j.renene.2022.08.124
Received 29 April 2022; Received in revised form 19 July 2022; Accepted 24 August 2022
Available online 30 August 2022

Nomenclature

CMC	Carboxymethylcellulose sodium
CSP	Concentrated solar power
FVM	Finite volume method
HTF	Heat transfer fluid
LHTES	Latent heat thermal energy storage
ORC	Organic Rankine Cycle
PCM	Phase change material
PV	Photovoltaic
REV	Representative elementary volume
SEM	Scanning Electron Microscopy
TER	Thermal energy release
TES	Thermal energy storage
A_s	Mushy zone constant
c_p	Specific heat capacity
d_{si}	Inner diameter of the shell
E	Thermal energy storage capacity
f_l	Liquid fraction
F_l	Inertial coefficient
g	Gravitational acceleration
H	Filling height of ceramic foam
k	Thermal conductivity
K	Permeability
L	Latent heat
m	Mass
p	Pressure
r_{si}, r_{so}	Inner and outer radius of the shell
r_{ti}, r_{to}	Inner and outer radius of the tube
t_m	Complete melting time
T	Temperature
$T_{initial}$, T_{in}	Initial temperature
T_{fin}	Final temperature
T_{m1}	The lower limit of melting point
T_{mu}	The upper limit of melting point
u, v, w	Velocity in x, y, z direction
$\vec{u}$	$\vec{U}$ Velocity
v_m	Solidification rate

Greek letters

ε	Porosity
ρ	Density
μ	Dynamic viscosity
β	Thermal expansion coefficient

Subscripts

E	Effective
F	Fluid
L	Lower
S	Solid skeleton
U	Upper
Por	Porous foam
HTF	Heat transfer fluid
PCM	Phase change material

discharging the energy stored in the storage tank. Pourmoghadam et al. [16] analysed the annual performance of a solar ORC integrated with LHTES where KNO_3–$NaNO_2$– $NaNO_3$ acted as PCM. Their results indicate that the closer the PCM melting temperature to the auxiliary heater setpoint temperature, the higher the energy and exergy efficiencies. Li et al. [17] conducted a thermal and economic analysis of a molten salt parabolic trough-based ORC integrated system. The effects of evaporation and condensation temperatures on the heat transfer areas were discussed to obtain cost-effective operation parameters.

However, almost all pure PCMs except metals suffer from low thermal conductivity [18]. For integrated solar power systems, the low thermal conductivity of molten salts affects the heat supply to the ORC sub-system and decreases the output power. Generally, there are three categories of methods to enhance the heat transfer at the PCM side: using fins, inserting porous foams and adding nanoparticles. Guo et al. [19] proposed to use angled fins to enhance the heat transfer of paraffin in a shell-and-tube LHTES unit. The inner tube was made of copper and annular fins were distributed on the outer surface of the copper tube. Numerical results indicate that the melting rate was increased by angled fins than the fins with large bending angles. Fins with 10° downward angle exhibited the best heat transfer enhancement. Huang et al. [20] designed tree-shaped fins to enhance the heat transfer of lauric acid. They found that the tree-shaped fins improved the temperature uniformity and charging/discharging rate. The effects of heat transfer fluid (HTF) temperature and flow rate were also discussed. The downward flow of HTF was beneficial to the discharging enhancement while the upward flow facilitated the charging improvement. Pu et al. [21] numerically studied the effect of copper foam on the thermal performance of paraffin. Multiple PCMs and gradient copper foams were utilised. The results indicate that the single PCM had better heat transfer effectiveness compared to radial multiple PCMs. The negative gradient metal foam showed better heat transfer enhancement than the positive and no gradient foams. The temperature distribution of the non-gradient type was the most uniform. Khatibi et al. [22] used different nanoparticles, i.e. Al_2O_3, ZnO, CuO and SiO_2, in a triplex-tube LHTES unit. They found that at the volume fraction of 2%, Al_2O_3-PCM had the highest discharging rate while at the volume fraction of 4%, the CuO-PCM had the highest discharging rate. Ge et al. [23] evaluated different heat transfer enhancement structures (finned tubes and metal foams) in a shell-and-tube LHTES unit. Paraffin was used as PCM and different filling ratios of metal foam were considered.

Although extensive studies have been carried out to enhance the heat transfer of pure PCMs, for molten salts, many current methods do not apply due to the serious corrosion and the extreme high-temperature environment. Ceramics have inherently high thermal conductivity, superior corrosion and high-temperature resistance [24–27]. But there are few studies evaluating the enhancement effect of ceramic foam on the discharging performance of molten salt, which leads to the lack of guidance on the potential application in solar power plants. Thus, in the current study, the open-cell ceramic foam was prepared and its anti-corrosion performance was tested experimentally. Then, a three-dimensional numerical model was developed to evaluate its discharging enhancement to molten salt in a shell-and-tube LHTES unit. Moreover, the effects of the foam filling position and filling height on discharging performance were analysed. Solar salt (40 wt% $NaNO_3$ + 60 wt% $NaNO_3$) is used as PCM and its melting point is 222.9–246.0 °C. The operating temperature range should at least cover the melting point so that the phase change of PCM occurs and thermal energy is stored in the form of latent heat. And the larger the temperature difference between PCM and HTF, the better the heat transfer [28,29]. During charging, the temperature of HTF should be much larger than 246.0 °C while during discharging, it should be much lower than 222.9 °C. This study quantitatively evaluates the discharging performance of ceramic foam-enhanced molten salt and provides guidance on designing thermal energy storage sub-system with excellent heat supply performance for solar power generation.

2. Experiments

2.1. Material preparation

The ceramic foam was fabricated using the dipping methods. The schematic of the preparation process is shown in Fig. 1. The polyurethane (PU) foam (pore density: 10 PPI) was supplied by Yueyang Sponge Co., Ltd. Industrial SiC ceramic powder (particle size:10 μm–13 μm) was used as the base material of the ceramic foam and purchased from Xianfeng Material Co., Ltd. Kaolin, alumina, yttrium oxide and polyvinyl alcohol were supplied by Yousuo Chemical Co., Ltd. Kaolin, alumina and yttrium oxide act as the sintering aids while polyvinyl alcohol was employed to improve the adhesion of the ceramic slurry to PU foams. N-octanol were purchased from Kermel Chemical Co., Ltd. $NaNO_3$ and KNO_3 (purity $\geq$99.0%) were supplied by China National Pharmaceutical Co., Ltd. The nitrate salts were utilised to prepare solar salt (60 wt% $NaNO_3$ + 40 wt% KNO_3) which is a widely used PCM in medium-temperature thermal energy storage.

First, the PU foam was submerged in NaOH solution (concentration: 10 wt%) for 12 h to activate the surface [30]. Then, it was dipped in the SiC ceramic slurry. The main components of the slurry are SiC powder, kaolin, alumina and yttrium oxide and the mass ratio is 86: 7: 4: 3. The mass fraction of these solid powders is 77.9%. In addition, carboxymethylcellulose sodium (CMC), sodium polyacrylate and N-octanol were added as the tackifier, dispersant and defoamer respectively. Silica sol and polyvinyl alcohol were added to improve the adhesion of the ceramic slurry to PU foams. The mass fractions of CMC, sodium polyacrylate, N-octanol, silica sol and polyvinyl alcohol are 17.8%, 0.2%, 0.1%, 3.7% and 0.3% respectively.

After dipping, the PU foams were dried at 80 °C for 6 h. Then, they were transferred into a furnace and sintered in the air atmosphere at 1400 °C for 2 h. After cooling, the ceramic foam was obtained. The porosity of the ceramic foam is about 0.85. It should be pointed out that the cubic-shaped ceramic foam was fabricated in the above process. Since the PU foam can be cut into various shapes, the annular-shaped ceramic foam can be fabricated and inserted into the annular space of the shell-and-tube unit.

2.2. Corrosion test

The anti-corrosion ability of the prepared ceramic was tested to ensure compatibility with molten salts. The bulk ceramic was sintered and was cut into pieces with the dimension of 10 × 10 × 2 mm, followed by polishing and drying. Subsequently, ceramic pieces were placed into alumina crucibles and buried by the solar salt. The crucibles were transferred into a furnace and heated from 150 °C to 300 °C with a heating rate of 10 °C/min. Then the temperature was kept at 300 °C for 30 min to melt the solar salt completely. Next, the temperature was decreased to 150 °C with a rate of 4 °C/min, followed by maintaining at 150 °C for 60 min. The above heating/cooling process is one charging/discharging cycle. Tests of 50, 100 and 200 charging/discharging cycles were carried out.

After the corrosion test, samples were washed using the flowing water to remove the salt on the surface. Then they were ultrasonically washed in the distilled water for 5 min to further remove the salt. Finally, they were dried at 40 °C for 3 h. The scanning electron microscope (SEM) was used to observe the surface morphology.

It is seen from Fig. 2(a) that there are many pores on the ceramic surface. The size of large pores is several tens microns while the size of the small pores is less than one micron. This morphology suggests that the ceramic itself has a porous structure. Compared with the reference ceramic (0 charging/discharging cycle), the global morphologies of tested ceramics do not change. And there are no cracks, layers or agglomerates [31,32] induced by chemical and mechanical damages. Moreover, even undergoing 200 charging/discharging cycles, the edges of ceramic grains are still sharp. These results suggest that the prepared ceramic possesses excellent corrosion resistance to solar salt.

3. Numerical modelling

3.1. Physical model

A 3D representative elementary volume (REV)-scale simulation [2] was performed to evaluate the discharging enhancement of the ceramic foam in a shell-and-tube LHTES unit. The physical model is shown in Fig. 3(a). The total length of the unit is 500 mm. The outer radius of the shell is 65 mm and the thickness is 3 mm. The outer radius of the tube is 22 mm and the thickness is 2 mm. The PCM with or without the ceramic foam occupies the annular space between the shell and the tube while HTF flows through the tube. The porosity of the ceramic foam is 0.85 and the pore density is 10 PPI.

11 points are selected to analyse the temperature response. The distribution of the monitored points is shown in Fig. 3(c). P1 – P5 are distributed horizontally and their coordinates are (22, 0), (32, 0), (42, 0), (52, 0) and (62, 0) respectively. P6 – P11 are distributed vertically and their coordinates are (0, 62), (0, 42), (0, 22), (0, −22), (0, −42) and (0, −62) respectively. All the points are in the $z = 250$ mm plane.

The effect of ceramic foam configurations on the discharging performance is also studied. First, the influence of the foam filling position is investigated. As shown in Fig. 3(d), the ceramic foams are inserted in the upper portion and the lower portion of the unit respectively. The filling height is 0.5 d_{si} (the inner diameter of the shell), i.e. $H_u = H_l = 62$ mm. Then, the effect of the filling height is studied by varying H_u or H_l. Selecting H_u or H_l depends on the best filling position.

For numerical modelling, the following assumptions were made: (1) the ceramic foam and PCM are homogenous and isotropic; (2) the flow of liquid PCM is laminar and incompressible; (3) the liquid PCM is subjected to the Boussinesq approximation; (4) the local thermal equilibrium exists between PCM and ceramic foam; (5) the volume difference of PCM before/after melting is neglected and (6) thermo-physical

Fig. 1. Schematic of the preparation process of the ceramic foam.

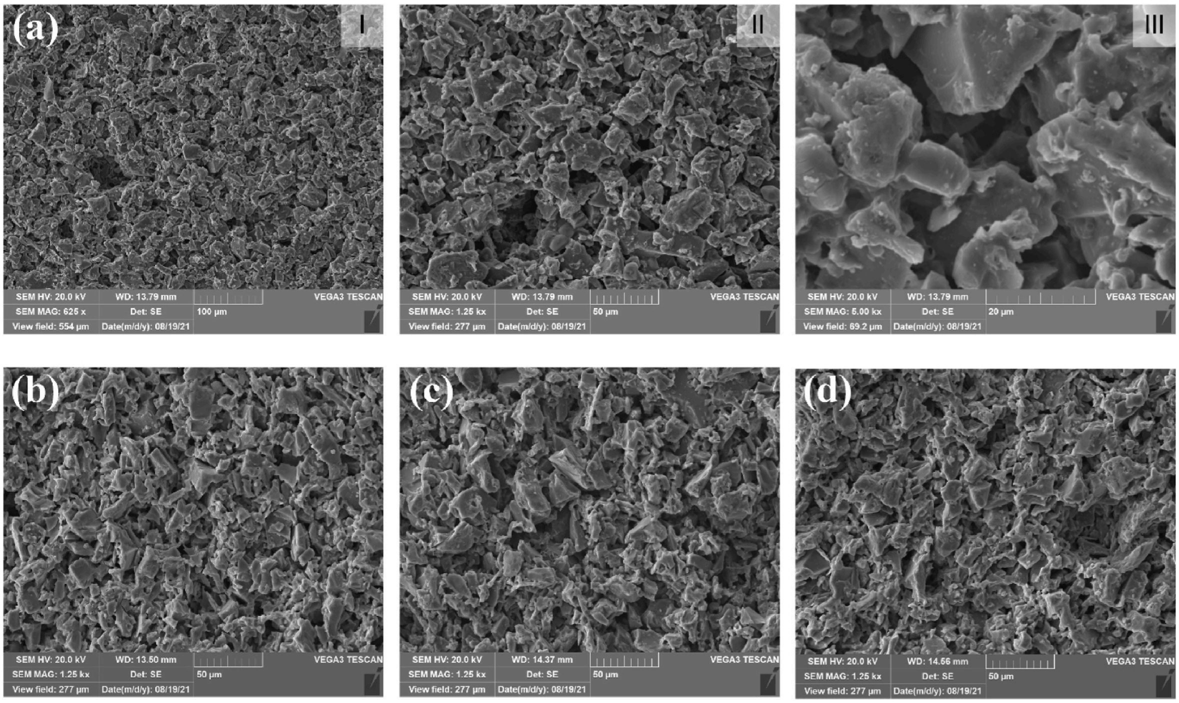

Fig. 2. Surface morphologies of ceramic pieces under (a) 0 charging/discharging cycle, (b) 50 cycles, (c) 100 cycles and (d) 200 cycles.

properties except PCM density are temperature-independent.

3.2. Governing equations

The governing equations for PCM are summarised as follows:
Continuity equation [33]:

$$\nabla \cdot \vec{U} = 0 \tag{1}$$

Momentum equations [34]:

$$\frac{\rho_f}{\varepsilon}\frac{\partial u}{\partial t}+\frac{\rho_f}{\varepsilon^2}\left(\vec{U}\cdot\nabla u\right) = -\frac{\partial p}{\partial x}-\frac{\mu_f}{K}u-\frac{\rho_f F_l}{\sqrt{K}}|u|u+\frac{\mu_f}{\varepsilon}\nabla^2 u - A_s u \tag{2}$$

$$\frac{\rho_f}{\varepsilon}\frac{\partial v}{\partial t}+\frac{\rho_f}{\varepsilon^2}\left(\vec{U}\cdot\nabla v\right) = -\frac{\partial p}{\partial y}-\frac{\mu_f}{K}v-\frac{\rho_f F_l}{\sqrt{K}}|v|v+\frac{\mu_f}{\varepsilon}\nabla^2 v-\rho_f\, g\,\beta\left(T_f-T_{m1}\right) - A_s v \tag{3}$$

$$\frac{\rho_f}{\varepsilon}\frac{\partial w}{\partial t}+\frac{\rho_f}{\varepsilon^2}\left(\vec{U}\cdot\nabla w\right) = -\frac{\partial p}{\partial z}-\frac{\mu_f}{K}w-\frac{\rho_f F_l}{\sqrt{K}}|w|w+\frac{\mu_f}{\varepsilon}\nabla^2 w - A_s w \tag{4}$$

where ρ_f is the fluid density; ε is the porosity; u, v and w are the velocities in x, y and z directions, respectively (assuming that the gravity is along - y direction); the second term on the right side of momentum equations accounts for the Darcy effect; the third and fourth term are the inertial resistance term and the flow resistance term respectively [35]; the fifth term on the right side of Eq. (3) denotes the natural convection driven by temperature difference; the last term is the superficial velocity source term to discriminate the solid-liquid region [36]. A_s is the mushy zone constant (10^5) [35].

The energy equation is [37]:

$$\left[(1-\varepsilon)\rho_s c_{ps}+\varepsilon\,\rho_f\,c_{pf}\right]\frac{\partial T}{\partial t}+\rho_f\,c_{pf}\left(\vec{U}\cdot\nabla T\right)=k_e\nabla^2 T-\varepsilon\rho L\frac{df_l}{dt} \tag{5}$$

where k_e is the effective thermal conductivity; c_{pf} and c_{ps} are the specific heat of PCM and the skeleton respectively; L is the latent heat; f_l is the liquid fraction. The liquid fraction quantifies the percentage of liquid PCM in the mushy zone and is evaluated as [38]:

$$f_l=\frac{T-T_{m1}}{T_{mu}-T_{ml}}=\begin{cases}0\,for\;T\;<\;T_{m1}\\ 0-1\,for\;T_{m1}\;\le\;T\;\le\;T_{mu}\\ 1\,for\;T\;>\;T_{mu}\end{cases} \tag{6}$$

where T_{ml} and T_{mu} are the lower and upper limits of the melting point of PCM.

For the HTF, forced convection occurs and the governing equations are [39]:

Continuity equation:

$$\nabla \cdot \vec{u} = 0$$

Momentum equation:

$$\rho_{HTF}\frac{\partial \vec{u}}{\partial t} + \rho_{HTF}(\vec{u}\cdot\nabla)\vec{u} = -\nabla p + \mu_{HTF}\nabla^2\vec{u} \tag{8}$$

Energy equation:

$$\rho_{HTF}\,c_{pHTF}\frac{\partial T}{\partial t} + \rho_{HTF}\,c_{pHTF}\,\vec{u}\cdot\nabla T = \nabla\cdot(k_{HTF}\nabla T) \tag{9}$$

where ρ_{HTF}, c_{pHTF} and k_{HTF} are density, specific heat and thermal conductivity of HTF.

3.3. Thermo-physical properties

Solar salt (60 wt% $NaNO_3$ + 40 wt% KNO_3) was used as PCM. Discovery DSC25 (TA Instruments Co., Ltd) was used to measure the melting point, latent heat and specific heat. The accuracy of the temperature control of the equipment is ±0.01 °C. The accuracy of the calorimeter (indium, the standard metal) is ±0.1%. The baseline reproducibility is < 40 μW. Thermal conductivity was measured using Hot Disk 2500S (Hot Disk AB Co., Ltd). The accuracy is ±3%. Other parameters are adopted from Ref. [40]. The thermo-physical properties of solar salt and ceramic are listed in Table 1.where k_s and k_f are the thermal conductivity of pure ceramic and PCM, respectively.

The permeability K and inertia coefficient F_l are calculated by Ref. [35]:

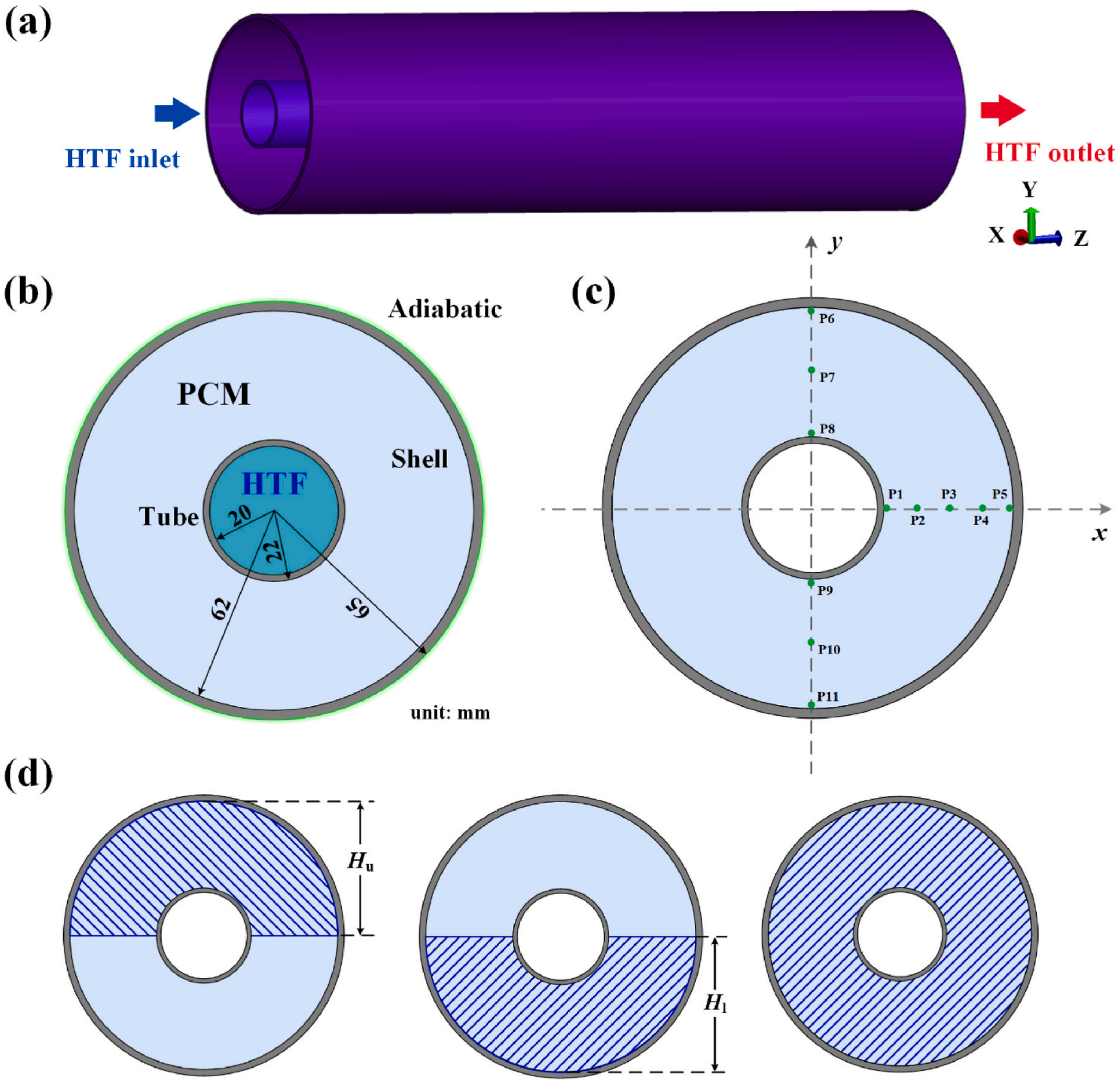

Fig. 3. (a) Physical model of the shell-and-tube unit used in the numerical study. (b) Dimension of the shell-and-tube unit. (c) Distribution of the monitored points. (d) Schematic of the upper foam-inserted unit, the lower foam-inserted unit and the fully foam-inserted unit ($H_u = H_l = 62$ mm).

$$K = \frac{\varepsilon^2\left(d_{fp}\sqrt{\kappa_{tor}/3\varepsilon}\right)^2}{36(\kappa_{tor} - 1)\kappa_{tor}} \tag{13}$$

$$F_l = 0.00212(1 - \varepsilon)^{-0.132}\left(d_{fs}/d_{fp}\right)^{-1.63} \tag{14}$$

$$d_{fp} = \frac{25.4 \times 10^{-3}}{PPI} \tag{15}$$

$$d_{fs} = 1.18\sqrt{\frac{1 - \varepsilon}{3\pi}}\left[\frac{1}{1 - e^{(\varepsilon-1)/0.04}}\right]d_{fp} \tag{16}$$

$$\frac{1}{\kappa_{tor}} = \frac{3}{4\varepsilon} + \frac{\sqrt{9 - 8\varepsilon}}{2\varepsilon}cos\left\{\frac{4\pi}{3} + \frac{1}{3}cos^{-1}\left[\frac{8\varepsilon^2 - 36\varepsilon + 27}{(9 - 8\varepsilon)^{1.5}}\right]\right\} \tag{17}$$

The material of the shell and the tube is AISI316 stainless steel [42] and HTF is the mineral oil [43,44]. Their properties are listed in Table 2.

3.4. Initial/boundary conditions

For the entire computational domain, the initial conditions are:

$$u = v = w = 0,\ T = T_{initial} \tag{18}$$

where T_{initial} is the initial temperature. T_{initial} is set as 270 °C which is 24 °C higher than the liquidus temperature of PCM.

The inlet temperature of HTF is 150 °C and the velocity is 0.05 m/s. The outlet boundary is set as Outflow to ensure the mass conservation. The outer wall of the shell, the front and back surface of the entire computing domain except the HTF domain are set as adiabatic.

At the interface between the tube and HTF:

$$T_{HTF} = T_{tube},\ (-k_{HTF}\nabla T_{HTF})\cdot n = (-k_{tube}\nabla T_{tube})\cdot n,\ u = v = w = 0 \tag{19}$$

At the interface between the tube and PCM:

$$T_{PCM} = T_{tube},\ (-k_{PCM}\nabla T_{PCM})\cdot n = (-k_{tube}\nabla T_{tube})\cdot n,\ u = v = w = 0 \tag{20}$$

At the interface between the shell and PCM:

$$T_{PCM} = T_{shell},\ (-k_{PCM}\nabla T_{PCM})\cdot n = (-k_{shell}\nabla T_{shell})\cdot n,\ u = v = w = 0 \tag{21}$$

$$k_{se} = \frac{1-\varepsilon}{3} k_s \tag{10}$$

$$k_{fe} = \frac{2+\varepsilon}{3} k_f \tag{11}$$

$$k_e = k_{fe} + k_{se} \tag{12}$$

Table 1
Thermo-physical properties of solar salt and ceramic.

Material	Parameter	Value
Solar salt	Density, kg/m^3	1980
	Latent heat, J/kg	140,000
	Melting point, °C	222.9–246.0
	Specific heat, J/kg K	1575
	Thermal conductivity (solid/liquid), W/m K	0.59/0.48
	Viscosity, mPa s	4.61
	Thermal expansion coefficient, K^{-1}	5.47×10^{-5}
Ceramic	Thermal conductivity, W/m K	20.7
	Specific heat, J/kg K	800
	Density, kg/m^3	2327

The effective thermal conductivity is calculated using the extended Lemlich model [41].

Table 2
Properties of shell/tube material and HTF.

Material	Parameter	Value
AISI316 stainless steel	Thermal conductivity, W/m K	16.2
	Specific heat, J/kg K	502
	Density, kg/m^3	8000
Mineral oil	Thermal conductivity, W/m K	0.1
	Specific heat, J/kg K	2436
	Viscosity, mPa s	1.085
	Density, kg/m^3	800

3.5. Numerical setup

ANSYS Fluent 18.0 package was used to solve the thermal transport problem. The finite volume method (FVM) was utilised to discretize the governing equations. The SIMPLE scheme was employed to couple pressure and velocity. The second-order upwind method was implemented to discretize pressure, momentum and energy terms. The under-relaxation factors were set as 0.3, 1, 1, 0.7, 0.9 and 1 for pressure, density, body forces, momentum, liquid fraction update and energy respectively. The convergence criteria for conservation equations of continuity, momentum and energy were 10^{-4}, 10^{-4} and 10^{-6} respectively.

Three mesh sets (1,093,935 cells, 1,218,366 cells and 1,847,104 cells) and time steps (0.5 s, 1 s and 2 s) were tested to balance the computational accuracy and time. First, under the fixed mesh of 1,218,366 cells, three time steps were tested. It is found that the time step almost has no influence on the liquid fraction over the whole discharging process. Thus, the time step of 2 s was adopted. Then, the three mesh sets were tested and the maximum difference in the liquid fraction was within 0.03. To save the computing resources, the mesh set of 1,218,366 cells was adopted.

3.6. Model validation

A previously published study was used to validate the current numerical model. Atal et al. [45] carried out an experimental study on the charging/discharging process of the paraffin/aluminium foam composite PCM in a shell-and-tube unit where air act as HTF. They also performed a 2D numerical simulation based on the experimental setup. The physical model is presented in Fig. 4(a). In the validation, the same physical model, thermos-physical properties, initial/boundary conditions were employed. The temperature at the monitored point, as indicated in Fig. 4(a), was compared. As seen in Fig. 4(b), the agreement on the general temperature trend is good. The deviation from the experimental results may lie in the difficulty in establishing the absolutely adiabatic boundary for the experiment, thus the experimental results are overall lower than the numerical results. The maximum deviation between the experimental and simulated results occurs at 141 min when the discharging begins in the simulation. The experimental temperature is 13.4 °C (19.7%) lower than the simulated result. After that, the deviation becomes smaller remarkably and at the end of discharging, the simulated results are almost the same as the experimental data. The currently simulated results are in good consistency with Atal et al.'s numerical results and the maximum difference is about 4%. Thus, the current numerical model is reliable.

4. Results and discussions

4.1. Comparison of liquid fraction

Fig. 5 shows the evolution of the liquid fraction in the four LHTES units. It is seen that the complete solidification time of the none foam-inserted unit is the longest (16626s). The addition of ceramic foam accelerates the solidification of PCM and the solidification in the fully foam-inserted unit is the fastest. The complete solidification time is 6780s. Considering the porosity (0.85), the solidification duration is shortened by 52.0% compared to the none foam-inserted unit. PCM in the lower foam-inserted unit solidifies faster than that in the upper foam-inserted unit before 3900s. However, the complete solidification time of the upper foam-inserted unit is shorter eventually (upper: 11194s; lower: 11670s). For the melting of PCM, the lower-inserted

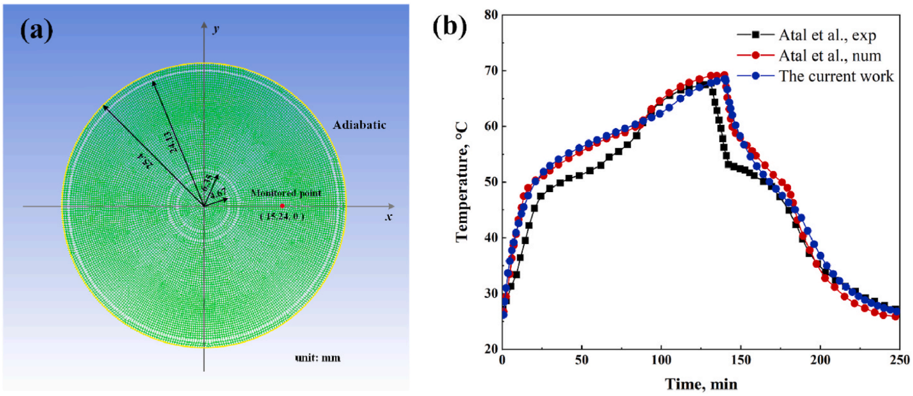

Fig. 4. (a) The location of the monitored point in Ref. [45]. (b) Transient temperature profiles between the current simulation and Ref. [45]. ("exp" and "num" denote "experimental results" and "numerical results" respectively).

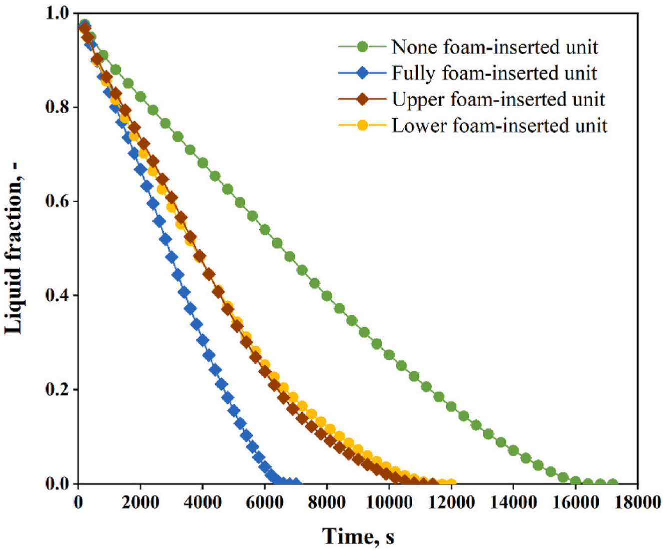

Fig. 5. Variation of liquid fraction with time in different configurations.

foam has a better enhancement than the upper-inserted foam [37]. However, for the solidification, the effect of the foam filling position is the opposite. The reasons will be analysed in the following sections.

4.2. Solidification front

The solidification front of PCMs in the four shell-and-tube units is presented in Fig. 6. For the none foam-inserted case, PCM near the tube first solidifies, then the solidification extends to the interior PCM. The shape of the solid-liquid interface is overall circular over the discharging process. This is different from the melting process where the solid-liquid interface is obviously deformed even at the initial stage [37]. PCM in the lower portion solidifies slightly faster than that in the upper portion. It should be attributed to natural convection: as seen in Fig. 7(a), PCM near the tube flows to the lower portion; due to the cooling effect of HTF, the temperature of this part of PCM is low, which accelerates the solidification in the lower portion.

For the fully foam-inserted unit, the solidification is obviously faster than the none foam-inserted unit. The shape of the solid-liquid interface is more circular. The solidification rates of the PCM in the upper and lower half are almost identical. This can be attributed to the restricted flow of liquid PCM by the porous skeleton. The velocity of PCM is smaller, as seen in Fig. 7(b), thus the influence of natural convection is lowered. The accelerated solidification is due to the enhanced heat conduction. The thermal conductivity of pure solar salt is 0.48 W/m K; the effective thermal conductivity of ceramic foam/solar salt is 1.49 W/m K. The enhancement of heat conduction exceeds the suppression of natural convection, as a result, the overall solidification is accelerated.

Regarding the upper foam-inserted case, the solidification of PCM in the upper half is obviously accelerated. This is understandable because the inserted ceramic foam increases the effective thermal conductivity of PCM in the upper half. It should be noted that, although there is no ceramic foam in the lower half, the solidification rate of PCM in this portion is faster than that in the none foam-inserted case. In other words, the inserted foam not only enhances the solidification in its own portion but makes a contribution to the other portion.

In terms of the lower foam-inserted case, the solidification front is opposite to the upper foam-inserted case. The solidification of PCM in the upper half is significantly slower than that in the lower half. However, the velocity of PCM in the upper half is larger, as seen in Fig. 7(d). This indicates that natural convection has an insignificant effect on solidification. For the melting process, the melting of PCM in the upper half can be faster than that in the lower half although the porous foam is inserted in the lower portion [46]. But for the current discharging process, the solidification rate of PCM in the upper half is always slower than that in the lower half. At 6000s and 8000s, the overall solidification is slightly slower than the upper foam-inserted case.

The variation of the solidification front along the axial direction is presented in Fig. 8. At 1000s and 2000s, the solidification front almost does not change with the axial position. With the elapse of time, the solidification of PCM at the outlet is slightly slower than that at the inlet. This is because HTF is heated by PCM and its temperature increases along the flow direction. So at the outlet, its cooling effect on PCM is lowered. At 6000s, the difference in the solidification front at the inlet and outlet is more significant. The solidification rate of PCM decreases along the flow direction of HTF.

4.3. Temperature response

Fig. 9 shows the temperature fields in different LHTES units. With regard to the none foam-inserted unit, the temperature of PCM which surrounds the tube is the lowest. And the temperature increases along the radial direction. The temperature of PCM in the upper half is higher than that in the lower half. This is due to natural convection, as discussed in Section 4.2. The temperature difference between this part of PCM and HTF is larger. So, if the ceramic foam is inserted in the upper portion, the discharging enhancement will be more significant. It may be the reason for the better discharging enhancement of the upper inserted foam, as observed in Fig. 5.

The overall temperature in the fully foam-insert unit is lower than that in the none foam-inserted unit. But at 2000s, 4000s and 6000s, the temperature of PCM which surrounds the tube is higher. This is because, in the fully foam-inserted unit, the cold energy is transferred to the interior PCM, rather than accumulating near the tube. In addition, the temperature distribution is more uniform in the fully foam-insert unit.

For the partially foam-inserted units, the ceramic foam decreases the local temperature. The temperature fields of the foam-inserted portion are nearly identical to that in the fully foam-inserted case. The temperature in the pure PCM portion is also decreased. This is because the cold PCM in the foam-inserted portion flows to the pure PCM portion, as Fig. 7 shows.

Fig. 10 shows the variation of temperature fields in the fully foam-inserted unit. At 1000s and 2000s, the axial position almost has no influence on the temperature fields, similar to the solidification front. As the time elapsed, there is a little difference in the temperature of PCM near the shell: the temperature of PCM at the outlet is slightly higher than that at the inlet. Since HTF is heated by PCM, its temperature increases along the flow direction. So, at the outlet, the temperature difference between HTF and PCM is decreased and the solidification of PCM becomes slow.

Fig. 11 shows the variation of the temperature at the monitored points. P1 – P5 are distributed horizontally and their distance from the tube increases in turn. It is found from Fig. 11(a) that the temperature of P1 decreases dramatically at the initial stage and then gradually. And the decreased magnitude of P1 is the largest. This is because P1 is closest to HTF and the cooling effect exerted on P1 is strongest.

When the ceramic foam is inserted into PCM, the temperature of P1 is increased, as Fig. 11(b) shows. But the temperature of P2 – P5 is decreased. Due to the increased effective thermal conductivity, the cold energy is efficiently transferred to the interior PCM, which should be responsible for the different temperature responses in the fully foam-inserted unit. Moreover, the temperature difference is decreased. For example, at the final discharging stage, the temperature difference between P1 and P5 is 45.8 °C while in the none foam-inserted unit, the temperature difference is 61.0 °C.

For the two partially foam-inserted units, it is seen from Fig. 11(c)–(d) that the variation of temperature at P1 – P5 is almost identical. Compared to the none foam-inserted case, the temperature difference is also decreased.

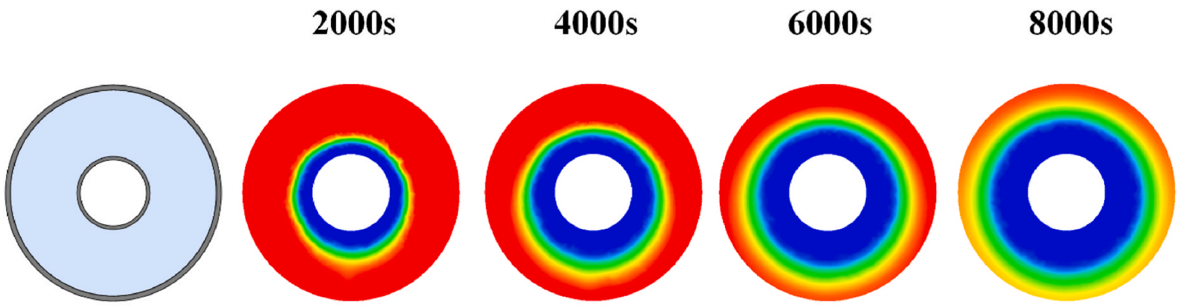

(a) none porous insert

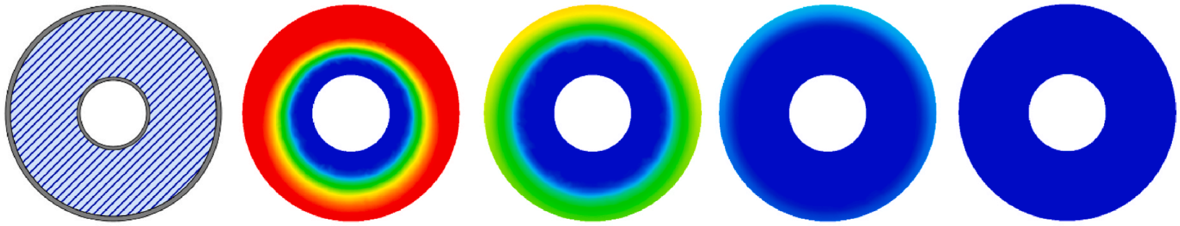

(b) full porous insert

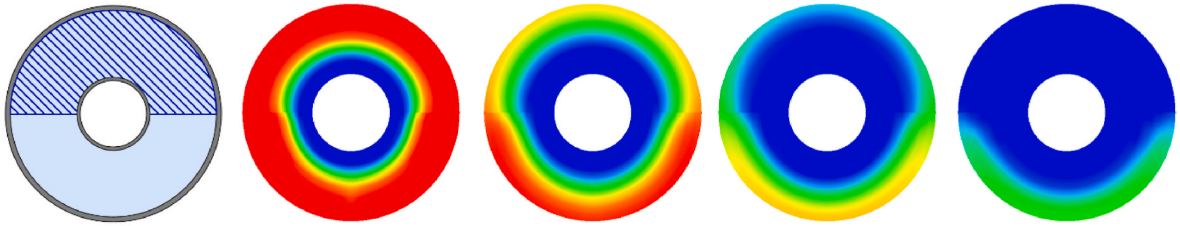

(c) upper porous insert

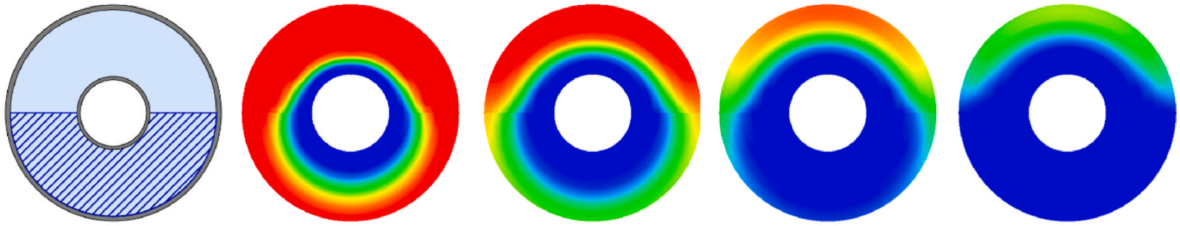

(d) lower porous insert

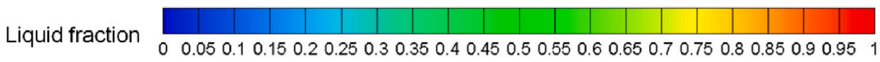

Fig. 6. Solidification front in the four LHTES units at 2000s, 4000s, 6000s and 8000s ($z = 250$ mm).

The variation of the temperature at monitored points P6 – P11 is presented in Fig. 12. As Fig. 12(a) shows, the temperature of P8 and P9 decreases fastest as the two points are closest to HTF. And the temperature of P9 is slightly lower than that of P8, which should be attributed to natural convection. The condition of P7/P10 and P6/P11 is the same. It should be noted that the temperature difference between P8 and P9 (also P7 and P10, P6 and P11) approaches 0 as the solidification proceeds. This may be because the fraction of liquid PCM decreases and the temperature reduces and thus the effect of natural convection gets insignificant. The trend of the temperature in the fully foam-inserted unit is similar to that in the none foam-inserted unit but the temperature difference between P6 and P9 is decreased.

When the ceramic foam is inserted into the upper half, at the initial stage, the temperature of P7 is higher than that of P10, which is the same as the none foam-inserted case. However, after 2700s, the temperature of P7 becomes lower than that of P10, as Fig. 12(c) shows. The condition of P6 and P11 is similar. It can be explained as follows: at the initial stage of discharging, the liquid fraction is large and the cold PCM flows to the lower portion, so the temperature of P7 is higher than that of P10; with the elapse of time, more PCM solidifies and most of them are in the upper portion, as Fig. 6(c) indicates; the solid (also cold) PCM cannot flow and is fixed in the upper portion, thus, the temperature of P7 becomes lower than that of P10.

In terms of the lower foam-inserted case, the temperature difference

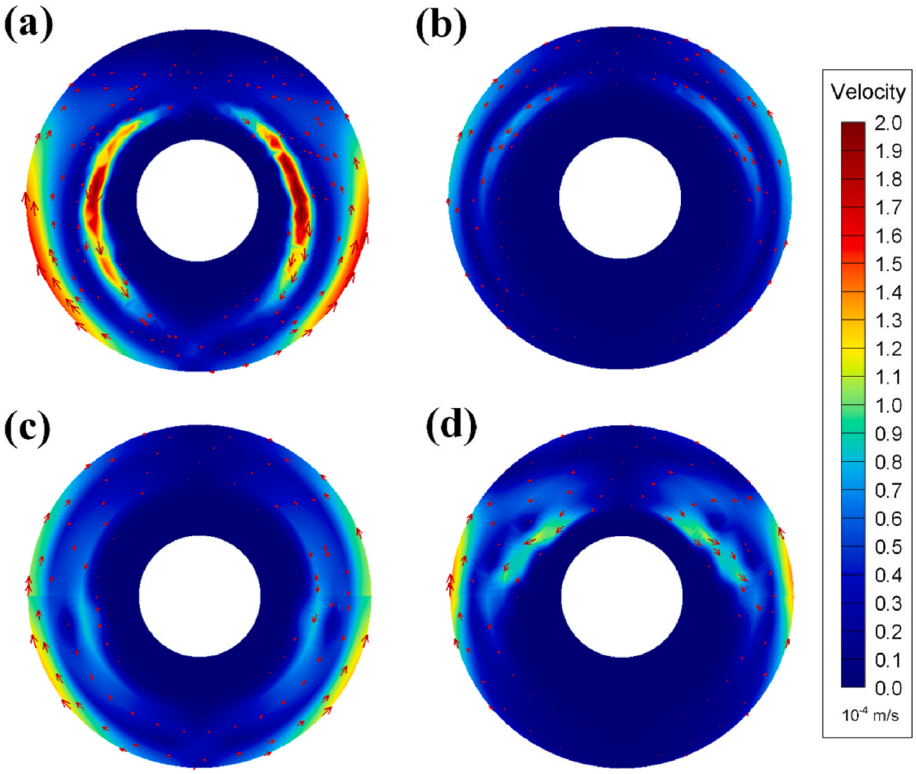

Fig. 7. Velocity fields in the four LHTES units at 2000s: (a) none foam-inserted unit; (b) fully foam-inserted unit; (c) upper foam-inserted unit; (d) lower foam-inserted unit.

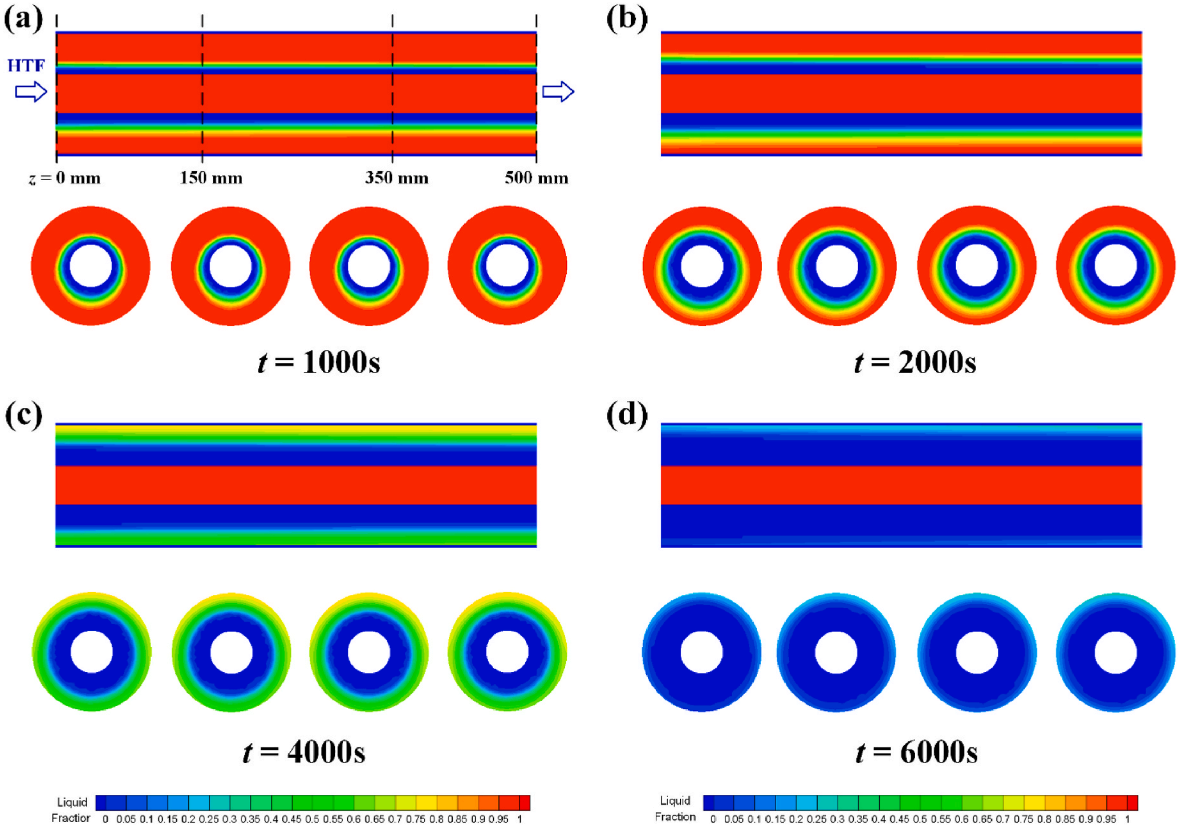

Fig. 8. Solidification front in the fully foam-inserted unit along the axial direction at different time.

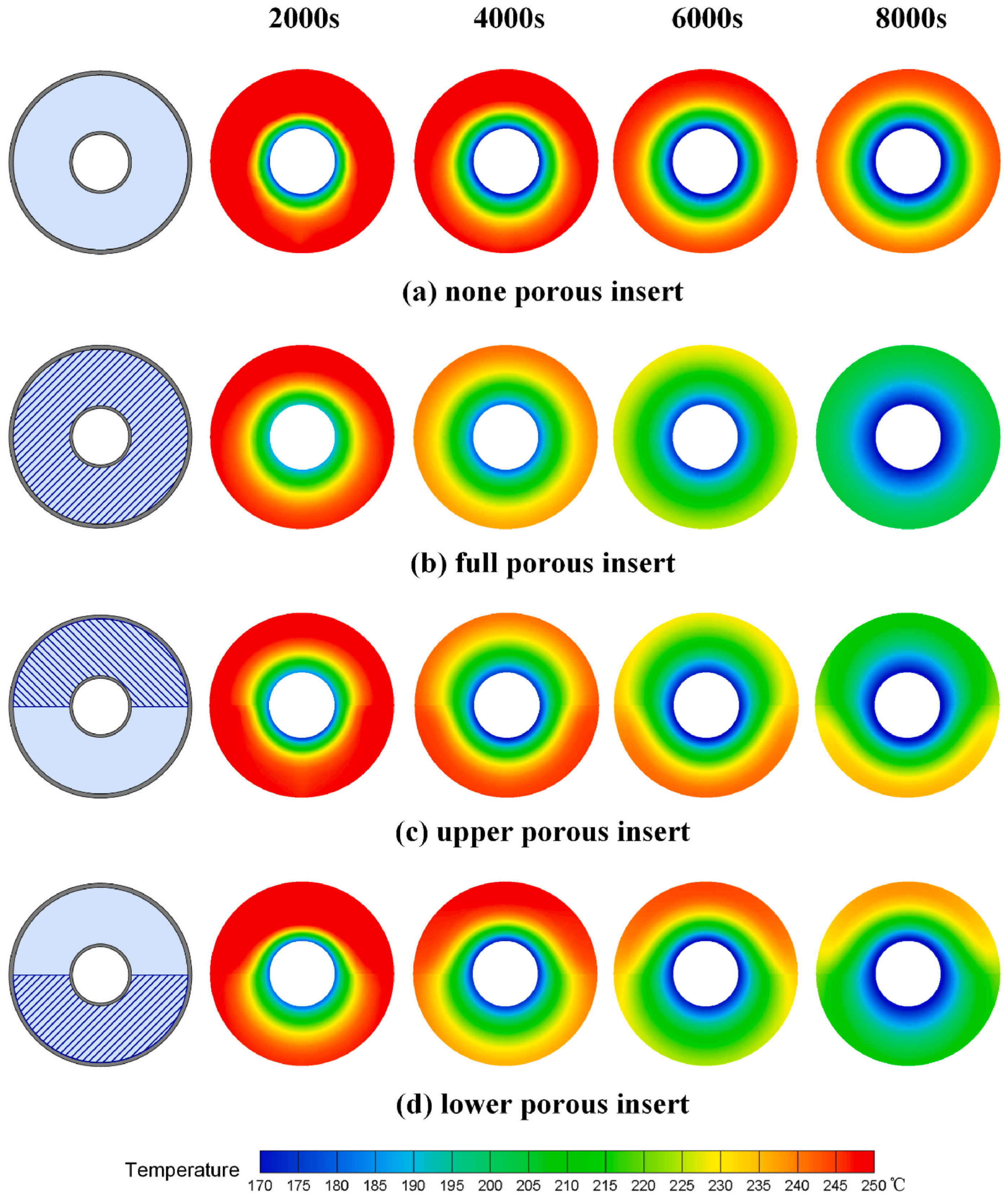

Fig. 9. Temperature fields in the four LHTES units at 2000s, 4000s, 6000s and 8000s ($z = 250$ mm).

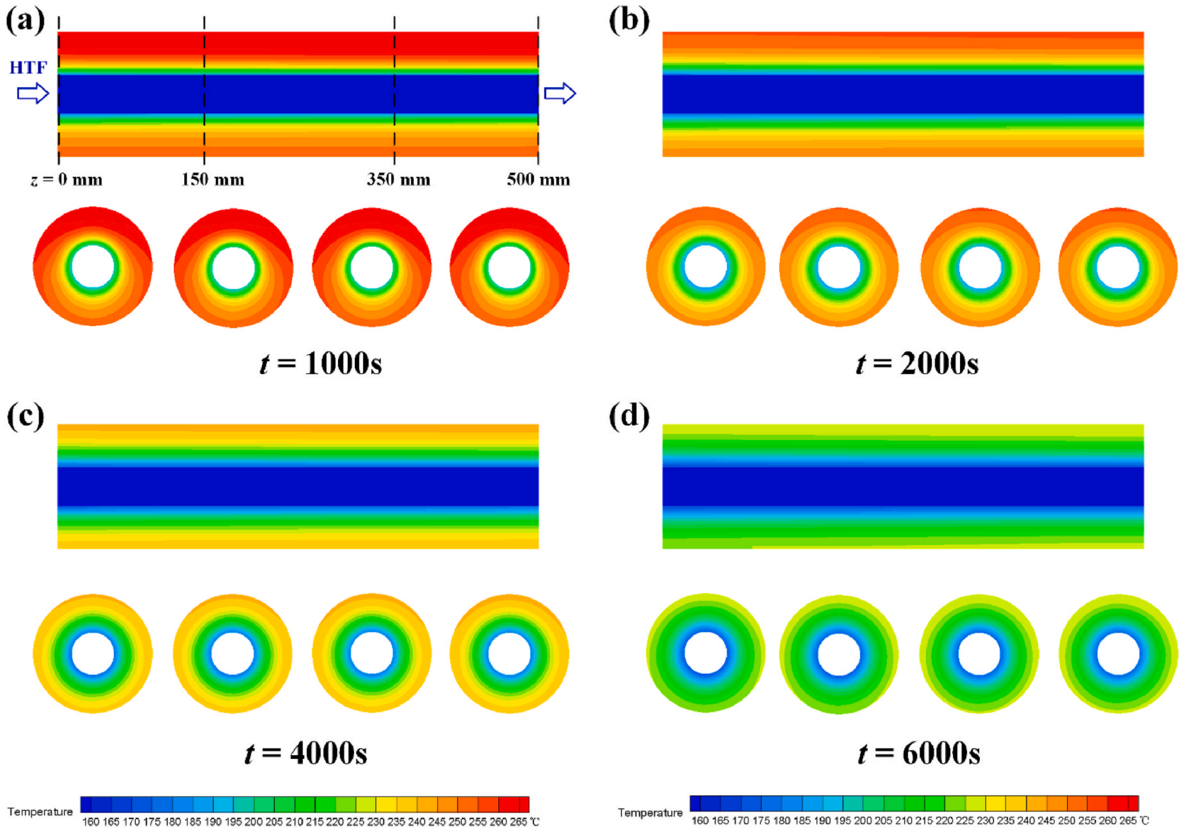

Fig. 10. Temperature fields in the fully foam-inserted unit along the axial direction at different time.

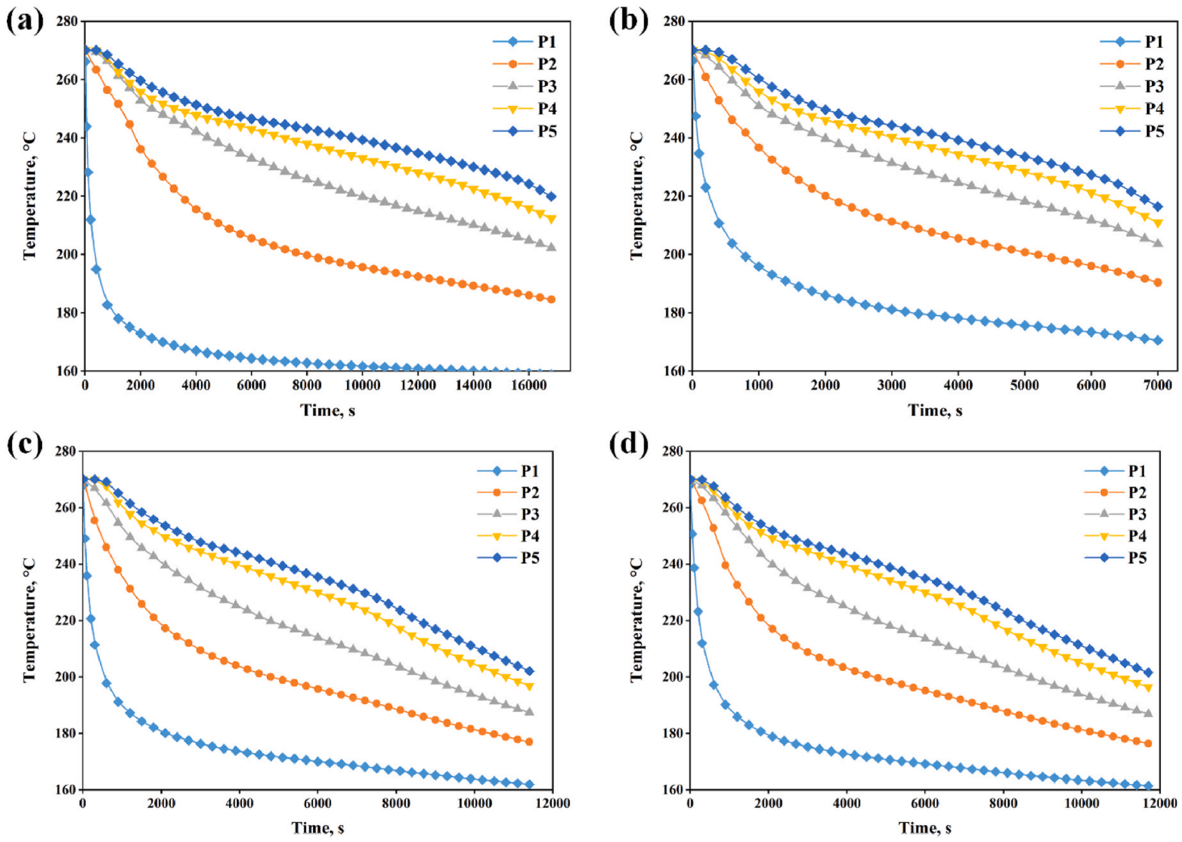

Fig. 11. Variation of the temperature of horizontally distributed points: (a) none foam-inserted unit; (b) fully foam-inserted unit; (c) upper foam-inserted unit; (d) lower foam-inserted unit.

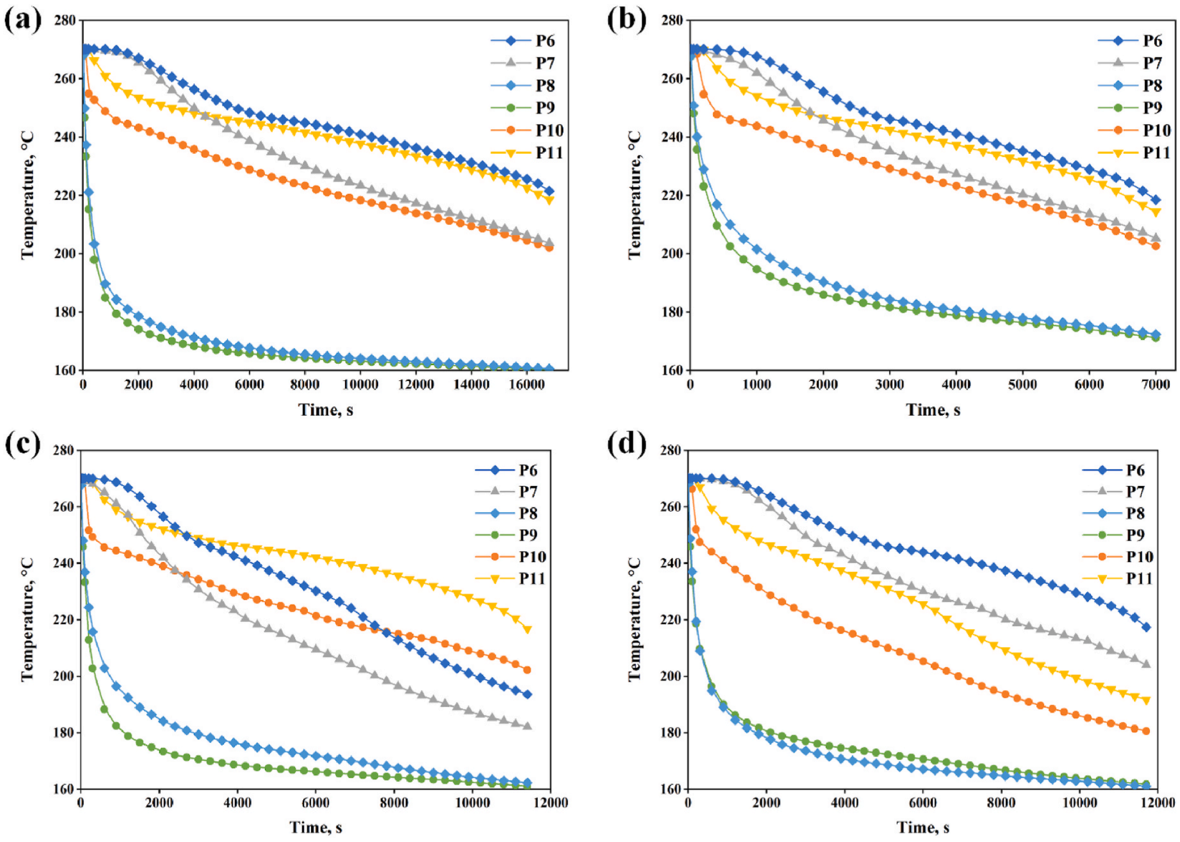

Fig. 12. Variation of the temperature of vertically distributed points: (a) none foam-inserted unit; (b) fully foam-inserted unit; (c) upper foam-inserted unit; (d) lower foam-inserted unit.

between P8 and P9 is nearly the same as that in the none foam-inserted case. However, the temperature difference between P7 and P10 does not approach 0 as the solidification proceeds. And the temperature difference between P6 and P11 even becomes larger. Due to the inserted ceramic foam, the effective thermal conductivity of PCM in the lower portion is increased, so the heat conduction is enhanced. In the middle and late stages, heat conduction dominates the solidification and PCM in the lower portion can absorb more cold from HTF. Thus, the temperature of P10 is greatly lower than that of P7.

4.4. Heat release performance

The amount of released thermal energy of the four units is plotted in Fig. 13. It is found that the fully foam-inserted unit releases heat fastest while the none foam-inserted unit does slowest. And the variation of the heat release rate of the upper and lower foam-inserted units is similar to the variation of liquid fraction, i.e. at the initial stage, the lower foam-inserted unit is faster while at the middle and late stages, the upper foam-inserted unit is faster. It is notable that the final amount of the released thermal energy is none > lower > upper > fully. This difference not only results from the fraction of PCM but from the final temperature. Since the cooling time of the four units is different, the final temperature is different. For example, the final average temperature of the fully foam-inserted unit is 203.5 °C while that of the lower foam-inserted unit is 190.4 °C. The different final temperature leads to the different amount of released sensible heat, which is one of the factors affecting the totally released thermal energy.

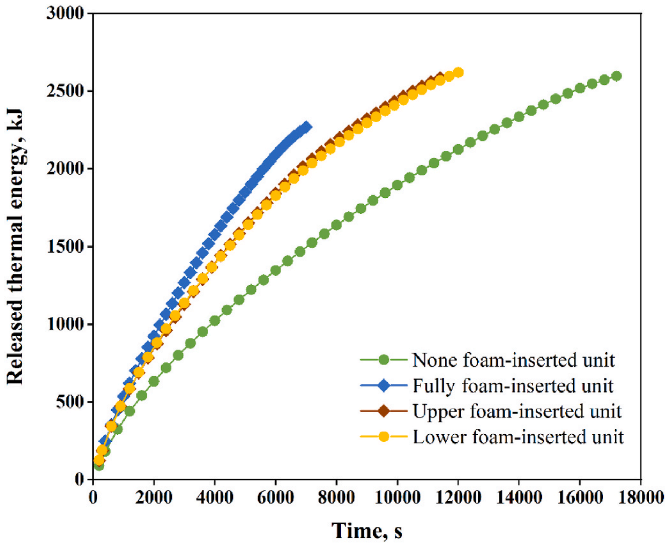

Fig. 13. Variation of the released thermal energy of the four configurations during the discharging.

To analyse the effect of foam filling height on the thermal energy release (TER) capacity, the final temperature of all the units are set as 200 °C. The ceramic foam is inserted in the upper portion because this configuration has a better discharging enhancement than the lower insert case. The foam filling height H_u ranges from 0.4 d_{si} to 1.0 d_{si}. 0.1 d_{si}, 0.2 d_{si} and 0.3 d_{si} are ignored due to the fact that the foam does not reach the tube and the tube cannot hold them. The TER capacity is calculated by Ref. [47]:

$$E = (T_{fin} - T_{ini}) m_{PCM} c_{p,PCM} + (T_{fin} - T_{ini}) m_{por} c_{p,por} + m_{PCM} L \tag{22}$$

where T_{fin} is the final average temperature of PCM; T_{ini} is the initial temperature; m_{PCM} and $c_{p,PCM}$ are the mass and the specific heat of PCM respectively; m_{por} and $c_{p,por}$ are the mass and the specific heat of porous ceramic foam respectively.

The solidification rate is calculated by:

$$v_m = \frac{1}{t_m} \tag{23}$$

where t_{m} is the complete solidification time.

Fig. 14 shows the variation of solidification rate and TER capacity with the foam filling height. The solidification rate increases with the filling height. This is understandable because the higher the filling height, the more the ceramic foam and the larger the effective thermal conductivity. It is noted that the solidification rate increases greatly as the filling height increases from 0.4 d_{si} to 0.9 d_{si}. When the filling height rises from 0.9 d_{si} to 1.0 d_{si}, the solidification rate increases slowly. The TER capacity decreases with the filling height because the fraction of PCM is decreased. And the decrease is generally linear.

To comprehensively evaluate the thermal energy release performance, the TER rate is calculated:

$$w = E \cdot v_m \tag{24}$$

where v_{m} is the solidification rate.

The TER rate considers both the solidification rate and TER capacity. It represents the amount of heat released unit time. The TES rates of units with different heights of foams are plotted in Fig. 15. It is seen that the TER rates of all the foam-inserted units are higher than that of the none foam-inserted unit. And the TER rate always increases with the increase of the foam filling height. The fully foam-inserted unit has the best comprehensive thermal energy release performance and the TER rate is 342.9 W, 118.1% higher than that of the none foam-inserted unit.

5. Conclusions

In this study, the ceramic foam was used to enhance the discharging performance of molten salt in a shell-and-tube latent heat thermal energy storage unit. The ceramic foam was fabricated and its corrosion resistance was confirmed experimentally. The three-dimensional numerical model was developed to evaluate the discharging performance of molten salt/ceramic foam composite phase change material. This study provides guidance on using ceramic foam to efficiently supply heat to generate electricity in solar power systems. The following conclusions are drawn:

(1) The addition of ceramic foam accelerates the solidification of molten salt. The fully foam-inserted unit has the fastest solidification rate, at which the complete solidification time can be shortened by 52.0%.
(2) The upper foam-inserted unit has a better discharging enhancement than the lower foam-inserted unit. This is because due to natural convection, the temperature of PCM in the upper portion is higher.
(3) Although the addition of ceramic foam decreases the thermal energy release capacity, it increases the discharging rate; and overall, the comprehensive discharging performance is improved. The thermal energy release rate of all the foam-inserted units is higher than that of the none foam-inserted unit.
(4) The thermal energy release rate always increases with the foam filling height. The thermal energy release rate of the fully foam-inserted unit is 118.2% higher than that of the none foam-inserted unit.

CRediT authorship contribution statement

Shuai Zhang: Conceptualization, Investigation, Methodology, Writing - original draft, Writing - review & editing. **Yuying Yan:** Conceptualization, Investigation, Supervision, Funding acquisition, Methodology, Writing - review & editing.

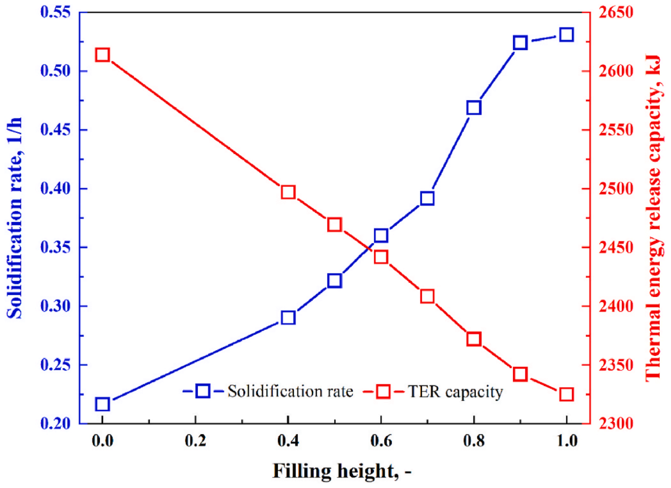

Fig. 14. Effect of the foam filling height on the solidification rate and thermal energy release capacity.

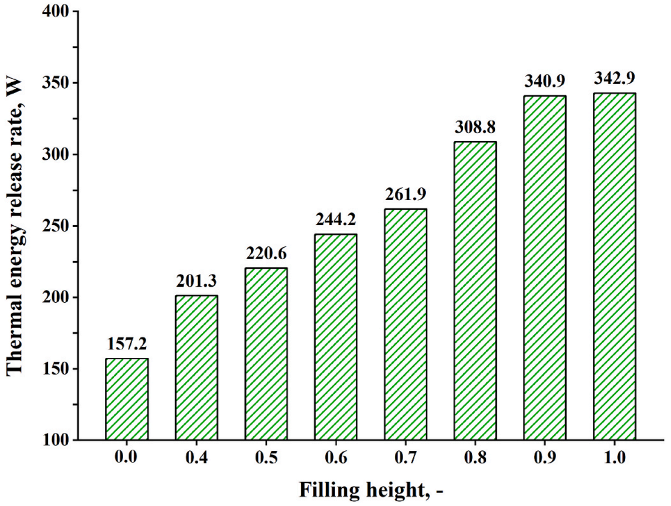

Fig. 15. Variation of the thermal energy release rate with the foam filling height.

Declaration of competing interest

The authors declare that they have no known competing financial interests or personal relationships that could have appeared to influence the work reported in this paper.

Acknowledgements

The authors would like to acknowledge the financial support by H2020-MSCA-RISE-778104–ThermaSMART, doctoral degree scholarship of China Scholarship Council (CSC). We are grateful for access to the University of Nottingham's Augusta HPC service.

References

[1] United Nations, Climate action. https://www.un.org/en/climatechange/net-zero-coalition, 2022.
[2] S. Zhang, D. Feng, L. Shi, L. Wang, Y. Jin, L. Tian, Z. Li, G. Wang, L. Zhao, Y. Yan, A review of phase change heat transfer in shape-stabilized phase change materials (ss-PCMs) based on porous supports for thermal energy storage, Renew. Sustain. Energy Rev. 135 (2021), 110127.

[3] S. Zhang, Z. Li, Y. Yao, L. Tian, Y. Yan, Heat transfer characteristics and compatibility of molten salt/ceramic porous composite phase change material, Nano Energy 100 (2022), 107476.

[4] H. Yu, H. Helland, X. Yu, T. Gundersen, G. Sin, Optimal design and operation of an Organic Rankine Cycle (ORC) system driven by solar energy with sensible thermal energy storage, Energy Convers. Manag. 244 (2021), 114494.

[5] E. Casati, A. Galli, P. Colonna, Thermal energy storage for solar-powered organic Rankine cycle engines, Sol. Energy 96 (2013) 205–219.

[6] U. Desideri, P.E. Campana, Analysis and comparison between a concentrating solar and a photovoltaic power plant, Appl. Energy 113 (2014) 422–433.

[7] X. Ju, C. Xu, Y. Hu, X. Han, G. Wei, X. Du, A review on the development of photovoltaic/concentrated solar power (PV-CSP) hybrid systems, Sol. Energy Mater. Sol. Cell. 161 (2017) 305–327.

[8] J. Yang, J. Li, Z. Yang, Y. Duan, Thermodynamic analysis and optimization of a solar organic Rankine cycle operating with stable output, Energy Convers. Manag. 187 (2019) 459–471.

[9] X. Li, H. Tian, G. Shu, M. Zhao, C.N. Markides, C. Hu, Potential of carbon dioxide transcritical power cycle waste-heat recovery systems for heavy-duty truck engines, Appl. Energy 250 (2019) 1581–1599.

[10] S. Zhang, Z. Li, H. Wang, L. Tian, Y. Jin, M. Alston, Y. Yan, Component-dependent Thermal Properties of Molten Salt Eutectics for Solar Thermal Energy Storage: Experiments, Molecular Simulation and Applications, Applied Thermal Engineering, 2022, 118333.

[11] V.R. Patil, V.I. Biradar, R. Shreyas, P. Garg, M.S. Orosz, N.C. Thirumalai, Techno-economic comparison of solar organic Rankine cycle (ORC) and photovoltaic (PV) systems with energy storage, Renew. Energy 113 (2017) 1250–1260.

[12] Z. Li, Y. Lu, R. Huang, J. Chang, X. Yu, R. Jiang, X. Yu, A.P. Roskilly, Applications and technological challenges for heat recovery, storage and utilisation with latent thermal energy storage, Appl. Energy 283 (2021), 116277.

[13] S. Zhang, Y. Jin, Y. Yan, Depression of melting point and latent heat of molten salts as inorganic phase change material: size effect and mechanism, J. Mol. Liq. 20 (2021), 117058.

[14] S. Zhang, Y. Yan, Melting and thermodynamic properties of nanoscale binary chloride salt as high-temperature energy storage material, Case Stud. Therm. Eng. 25 (2021), 100973.

[15] L. Cioccolanti, R. Tascioni, A. Arteconi, Mathematical modelling of operation modes and performance evaluation of an innovative small-scale concentrated solar organic Rankine cycle plant, Appl. Energy 221 (2018) 464–476.

[16] P. Pourmoghadam, M. Farighi, F. Pourfayaz, A. Kasaeian, Annual transient analysis of energetic, exergetic, and economic performances of solar cascade organic Rankine cycles integrated with PCM-based thermal energy storage systems, Case Stud. Therm. Eng. 28 (2021), 101388.

[17] J.F. Li, H. Guo, Q.P. Meng, Y.T. Wu, F. Ye, C.F. Ma, Thermoeconomic analysis on a molten salt parabolic trough-based concentrated solar organic Rankine cycle system, Int. J. Energy Res. 44 (2020) 3395–3411.

[18] N.I. Ibrahim, F.A. Al-Sulaiman, S. Rahman, B.S. Yilbas, A.Z. Sahin, Heat transfer enhancement of phase change materials for thermal energy storage applications: a critical review, Renew. Sustain. Energy Rev. 74 (2017) 26–50.

[19] J. Guo, Z. Liu, B. Yang, X. Yang, J. Yan, Melting assessment on the angled fin design for a novel latent heat thermal energy storage tube, Renew. Energy 183 (2022) 406–422.

[20] Y. Huang, X. Liu, Charging and discharging enhancement of a vertical latent heat storage unit by fractal tree-shaped fins, Renew. Energy 174 (2021) 199–217.

[21] L. Pu, S. Zhang, L. Xu, Z. Ma, X. Wang, Numerical study on the performance of shell-and-tube thermal energy storage using multiple PCMs and gradient copper foam, Renew. Energy 174 (2021) 573–589.

[22] M. Khatibi, R. Nemati-Farouji, A. Taheri, A. Kazemian, T. Ma, H. Niazmand, Optimization and performance investigation of the solidification behavior of nano-enhanced phase change materials in triplex-tube and shell-and-tube energy storage units, J. Energy Storage 33 (2021), 102055.

[23] R. Ge, Q. Li, C. Li, Q. Liu, Evaluation of Different Melting Performance Enhancement Structures in a Shell-And-Tube Latent Heat Thermal Energy Storage System, Renewable Energy, 2022.

[24] R. Fukahori, T. Nomura, C. Zhu, N. Sheng, N. Okinaka, T. Akiyama, Thermal analysis of Al–Si alloys as high-temperature phase-change material and their corrosion properties with ceramic materials, Appl. Energy 163 (2016) 1–8.

[25] Y. Zhao, H.B. Liu, C.Y. Zhao, Experimental study on the cycling stability and corrosive property of Al-Si alloys as phase change materials in high-temperature heat storage, Sol. Energy Mater. Sol. Cell. 203 (2019), 110165.

[26] H. Xu, F. Dal Magro, N. Sadiki, J.-M. Mancaux, X. Py, A. Romagnoli, Compatibility study between aluminium alloys and alternative recycled ceramics for thermal energy storage applications, Appl. Energy 220 (2018) 94–105.

[27] I. Ortega-Fernández, Y. Grosu, A. Ocio, P.L. Arias, J. Rodríguez-Aseguinolaza, A. Faik, New insights into the corrosion mechanism between molten nitrate salts and ceramic materials for packed bed thermocline systems: a case study for steel slag and Solar salt, Sol. Energy 173 (2018) 152–159.

[28] M. Avci, M.Y. Yazici, Experimental study of thermal energy storage characteristics of a paraffin in a horizontal tube-in-shell storage unit, Energy Convers. Manag. 73 (2013) 271–277.

[29] N.R. Vyshak, G. Jilani, Numerical analysis of latent heat thermal energy storage system, Energy Convers. Manag. 48 (2007) 2161–2168.

[30] F. Ren, Z. Wang, Z. Ma, J. Su, F. Li, L. Wang, Effects of Fe2O3 concentration on microstructures and properties of SiC-based ceramic foams, Mater. Sci. Eng., A 515 (2009) 113–116.

[31] F. Motte, Q. Falcoz, E. Veron, X. Py, Compatibility tests between Solar Salt and thermal storage ceramics from inorganic industrial wastes, Appl. Energy 155 (2015) 14–22.

[32] Y. Qin, X. Li, C. Liu, C. Zheng, Q. Mao, B. Chen, K. Jing, Y. Tan, L. Cheng, L. Zhang, Effect of deposition temperature on the corrosion behavior of CVD SiC coatings on SiCf/SiC composites under simulated PWR conditions, Corrosion Sci. 181 (2021), 109233.

[33] W.Q. Li, Z.G. Qu, Y.L. He, W.Q. Tao, Experimental and numerical studies on melting phase change heat transfer in open-cell metallic foams filled with paraffin, Appl. Therm. Eng. 37 (2012) 1–9.

[34] Z.G. Qu, W.Q. Li, W.Q. Tao, Numerical model of the passive thermal management system for high-power lithium ion battery by using porous metal foam saturated with phase change material, Int. J. Hydrogen Energy 39 (2014) 3904–3913.

[35] Y. Yao, H. Wu, Macroscale modeling of solid–liquid phase change in metal foam/paraffin composite: effects of paraffin density treatment, thermal dispersion, and interstitial heat transfer, J. Therm. Sci. Eng. Appl. (2021) 13.

[36] V. Joshi, M.K. Rathod, Thermal performance augmentation of metal foam infused phase change material using a partial filling strategy: an evaluation for fill height ratio and porosity, Appl. Energy 253 (2019), 113621.

[37] Y. Xu, Q. Ren, Z.-J. Zheng, Y.-L. He, Evaluation and optimization of melting performance for a latent heat thermal energy storage unit partially filled with porous media, Appl. Energy 193 (2017) 84–95.

[38] M. Caliano, N. Bianco, G. Graditi, L. Mongibello, Analysis of a phase change material-based unit and of an aluminum foam/phase change material composite-based unit for cold thermal energy storage by numerical simulation, Appl. Energy 256 (2019), 113921.

[39] X. Yang, P. Wei, X. Wang, Y.-L. He, Gradient design of pore parameters on the melting process in a thermal energy storage unit filled with open-cell metal foam, Appl. Energy 268 (2020), 115019.

[40] A. Anagnostopoulos, A. Alexiadis, Y. Ding, Molecular dynamics simulation of solar salt (NaNO3-KNO3) mixtures, Sol. Energy Mater. Sol. Cell. 200 (2019), 109897.

[41] Y. Yao, H. Wu, Interfacial heat transfer in metal foam porous media (MFPM) under steady thermal conduction condition and extension of Lemlich foam conductivity theory, Int. J. Heat Mass Tran. 169 (2021), 120974.

[42] Q. Zhang, D. Cao, Z. Ge, X. Du, Response characteristics of external receiver for concentrated solar power to disturbance during operation, Appl. Energy 278 (2020), 115709.

[43] M. Medrano, A. Gil, I. Martorell, X. Potau, L.F. Cabeza, State of the art on high-temperature thermal energy storage for power generation. Part 2—case studies, Renew. Sustain. Energy Rev. 14 (2010) 56–72.

[44] K. Vignarooban, X. Xu, A. Arvay, K. Hsu, A.M. Kannan, Heat transfer fluids for concentrating solar power systems – a review, Appl. Energy 146 (2015) 383–396.

[45] A. Atal, Y. Wang, M. Harsha, S. Sengupta, Effect of porosity of conducting matrix on a phase change energy storage device, Int. J. Heat Mass Tran. 93 (2016) 9–16.

[46] Y. Xu, M.-J. Li, Z.-J. Zheng, X.-D. Xue, Melting performance enhancement of phase change material by a limited amount of metal foam: configurational optimization and economic assessment, Appl. Energy 212 (2018) 868–880.

[47] C. Yang, Y. Xu, X. Cai, Z.-J. Zheng, Melting behavior of the latent heat thermal energy storage unit with fins and graded metal foam, Appl. Therm. Eng. 198 (2021), 117462.